Nanoscale

PAPER

View Article Online
View Journal | View Issue

Cite this: *Nanoscale*, 2024, **16**, 10618

Perovskite $CoSn(OH)_6$ nanocubes with tuned d-band states towards enhanced oxygen evolution reactions†

Mingwei Sun,[a,b] Baopeng Yang,[c] Jiaxing Yan,[b] Yulong Zhou,[b] Zhencong Huang,[b] Ning Zhang, *[b] Rong Mo*[a] and Renzhi Ma *[d]

Received 7th March 2024,
Accepted 26th April 2024

DOI: 10.1039/d4nr00975d

rsc.li/nanoscale

The $CoSn(OH)_6$ perovskite hydroxide is a structure stable and inexpensive electrocatalyst for the oxygen evolution reaction (OER). However, the OER activity of $CoSn(OH)_6$ is still unfavorable due to its limited active sites. In this work, an Fe^{3+} doping strategy is used to optimize the d-band state of the $CoSn(OH)_6$ perovskite hydroxide. The $CoSn(OH)_6$ catalyst with slightly Fe^{3+} doped nanocubes is synthesized by a facile hydrothermal method. Structure characterization shows that Fe^{3+} ions are incorporated into the crystal structure of $CoSn(OH)_6$. Owing to the regulation of the electronic structure, $CoSn(OH)_6$-Fe1.8% exhibits an OER overpotential of 289 mV at a current density of 10 mA cm^{-2} in OER electrochemical tests. *In situ* Raman spectroscopy shows that no obvious re-construction occurred during the OER for both $CoSn(OH)_6$ and $CoSn(OH)_6$-Fe1.8%. DFT calculations show that the introduction of Fe^{3+} into $CoSn(OH)_6$ can shift the d-band center to a relatively high position, thus promoting the OER intermediates' adsorption ability. Further DFT calculations suggest that incorporation of an appropriate amount of Fe^{3+} into $CoSn(OH)_6$ significantly reduces the rate-determining Gibbs free energy during the OER. This work offers valuable insights into tuning the d-band center of perovskite hydroxide materials for efficient OER applications.

1. Introduction

The intensifying energy crisis, driven by excessive fossil fuel consumption, is becoming more serious.[1,2] In response to this challenge, electrochemical water decomposition has gained widespread attention as a sustainable energy conversion technology.[3,4] The electrocatalytic process of water decomposition to produce hydrogen is seen as a promising technique achieving green and sustainable hydrogen energy.[5,6] The main challenge in this process lies in the high dynamic barrier of the four-electron-transfer oxygen evolution reaction (OER) at the anode.[7] Currently, precious metal-based catalysts like RuO_2 and IrO_2 are considered benchmarks for industrial OER catalysts.[5,8] However, their limited reserves and high costs constrain their commercial application.[9–11] Therefore, the development of durable, stable, and highly active non-noble metal electrocatalysts holds great significance in addressing these challenges.[12,13]

Non-precious transition-metal-based catalysts such as phosphates, sulfides, nitrides, and hydroxides have received much attention due to their inexpensiveness, abundance, and unique electrochemical properties.[14–18] Among them, transition metal hydroxides, such as layered transition metal hydroxides (*e.g.* $Co(OH)_2$, $Ni(OH)_2$, $Ni_xFe_{1-x}(OH)_2$ *etc.*), have been widely studied as electrocatalysts for the OER.[19–21] However, the layered transition metal hydroxides are easily converted into oxyhydroxides during the OER process, which possibly causes their instability and reduced activity.[22,23] The perovskite type hydroxides, such as $CoSn(OH)_6$, $MgSn(OH)_6$, $CdSn(OH)_6$, *etc.*, also have attracted attention.[24] The perovskite type hydroxides are chemically stable, and usually show relatively inert phase transformation to oxyhydroxides during the OER process.[25] Furthermore, the perovskite structure and the contained special metals such as Sn, Ti, Fe, and Co can bring special electronic structures, which will enable unique electrochemical behaviors.[26] As a typical perovskite hydroxide, $CoSn(OH)_6$ has electrochemical activity and a stable chemical structure, and is widely studied as an electrocatalyst for the OER.

[a]*Hunan Key Laboratory for Micro–Nano Energy Materials and Devices, School of Physics and Optoelectronics, Xiangtan University, Hunan 411105, P. R. China. E-mail: morong@xtu.edu.cn*
[b]*School of Materials Science and Engineering, Central South University, Changsha 410083, China. E-mail: nzhang@csu.edu.cn*
[c]*School of Physics and Electronics, Central South University, Changsha 410083, China*
[d]*Research Center for Materials Nanoarchitectonics (MANA), National Institute for Materials Science (NIMS), 1-1 Namiki, Tsukuba, Ibaraki 305-0044, Japan. E-mail: ma.renzhi@nims.go.jp*
†Electronic supplementary information (ESI) available. See DOI: https://doi.org/10.1039/d4nr00975d

For example, Chen *et al.* reported that the $CoSn(OH)_6$ perovskite hydroxide with Sn vacancies shows improved adsorption and electron transfer during the electrocatalytic OER process.[27] Wang *et al.* reported single-crystal $CoSn(OH)_6$ nanoboxes with a porous shell for improved OER properties.[28] Liu and co-workers demonstrated that $CoSn(OH)_6$ can be transformed into amorphous $CoSnO_x$ materials, which have promoted the OER process.[24] Although these processes have been achieved with perovskite structure materials, the OER activity of perovskite $CoSn(OH)_6$ materials is still too low to be applied in practical water splitting.[29]

Modulating the electronic d-band center of catalysts has been realized as one of the most effective strategies to optimize the energy of the binding intermediates.[30–34] Precisely controlling the location, width, and electron count of the d-band center enables adjustment of intermediates' adsorption strength and reactivity, thereby optimizing the performance of OER catalysts.[35,36] For instance, NiO exogenously doped with Li^+,[37] $Ni_3Ge_2O_5(OH)_4$ with doped Fe^{3+},[38] and Ni–Fe layered double hydroxides (LDH) with doped Ce^{3+} have been developed to optimize the d-band states for efficient OER applications.[39] Unfortunately, tuning the d-band center of perovskite based electrocatalytic materials has been seldom reported yet.

In this work, $CoSn(OH)_6$ nanocubes with a tuned d-band center were synthesized for promoting OER behaviors. The $CoSn(OH)_6$ nanocubes with different amounts of doped Fe^{3+} were synthesized by a simple hydrothermal process. X-Ray diffraction (XRD) spectroscopy, scanning electron microscopy (SEM), transmission electron microscopy (TEM), energy dispersive X-ray spectroscopy (EDX), and X-Ray photoelectron spectroscopy (XPS) prove that the crystal structure, morphology and chemical composition of the $CoSn(OH)_6$ nanocubes with proper Fe^{3+} doped. During the electrocatalytic measurements, $CoSn(OH)_6$ doped with 1.8 wt% Fe^{3+} exhibited optimized OER activity to deliver 10 mA cm^{-2} at an overpotential of 289 mV. Such a performance is much superior to that of the corresponding pristine $CoSn(OH)_6$. To further reveal the intrinsic mechanism of the OER behaviors of these materials, the electronic states of the d-band are calculated using density functional theory (DFT). With the increase of the doping content of Fe^{3+}, the d-band center of $CoSn(OH)_6$ increased. Such a change brought easier adsorption of OER intermediates. The work reported here has given a facile and efficient strategy to promote the OER activity of perovskite transition metal-based hydroxides.

2. Experimental

2.1 Synthesis of $CoSn(OH)_6$

Nanocrystals of the perovskite hydroxide $CoSn(OH)_6$ were prepared by a hydrothermal method. In a typical procedure, Na_2SnO_3 (1.0 mmol) and $CoCl_2{\cdot}6H_2O$ (1.5 mmol) were dissolved in 20 mL of deionized water separately. Then, the above solutions were mixed and stirred for 10 min. Afterward, the mixed solution was transferred into a sealed Teflon-lined stainless-steel autoclave and subsequently heated in an electronic oven at 200 °C for 24 h. After cooling to room temperature, the products were washed several times using distilled water and ethanol. Finally, the products were dried at 60 °C for 12 h. The obtained powders were collected and ground into a fine powder.

2.2 Synthesis of Fe^{3+} doped $CoSn(OH)_6$

The $CoSn(OH)_6$ doped with Fe^{3+} was prepared by the same process as that for $CoSn(OH)_6$. The difference was that the $CoCl_2{\cdot}6H_2O$ solution was replaced by different amounts of mixed solution of $FeCl_3{\cdot}6H_2O$ and $CoCl_2{\cdot}6H_2O$ in 15 mL of deionized water with the Fe to Co ratios of 0 at%, 2 at%, 5 at%, and 8 at%. The exact composition of Fe, Sn, and Co was confirmed by inductively coupled plasma-optical emission spectrometry (ICP-OES) results as shown in Table S1†. According to the ICP-OES measurements, the as-prepared products were denoted as $CoSn(OH)_6$, $CoSn(OH)_6$-Fe0.9%, $CoSn(OH)_6$-Fe1.8%, and $CoSn(OH)_6$-Fe2.7%, respectively.

More experimental details are available in the ESI.†

3. Results and discussion

3.1 Structure characterization

A series of perovskite hydroxides doped with different amounts of Fe^{3+} were synthesized by hydrothermal methods. The crystal composition of the prepared products was further analyzed by the XRD technique. As shown in Fig. 1a, the XRD peaks of the products are finely indexed to the perovskite $CoSn(OH)_6$ (JCPDS no. 13-0356), suggesting that $CoSn(OH)_6$ materials have been successfully synthesized. The enlarged figure displays the high-resolution image of (200) peaks. It is shown that the (200) peak is shifted to a smaller angle as the Fe^{3+} doping concentration increased. Such a phenomenon is caused because Fe^{3+} has a larger anion radius than Co^{3+} and the cell lattice volume is expanded after doping.[40]

Fig. 1b shows the scanning electron microscopy (SEM) image of pure $CoSn(OH)_6$. It is observed that the pristine $CoSn(OH)_6$ material was cube shaped with a size of about 60 nm. After Fe^{3+} doping, the SEM images display that $CoSn(OH)_6$-Fe0.9%(Fig. 1c), $CoSn(OH)_6$-Fe1.8%(Fig. 1d), and $CoSn(OH)_6$-Fe2.7% (Fig. 1e) have overall maintained the cube-like morphology.[24] With the amount of doped Fe^{3+} increasing, the cube-like morphology becomes more irregular (Fig. S1†). Moreover, the corresponding energy dispersive spectrometry (EDX) was performed to further analyze the elemental percentage data of the as-prepared materials. As the EDX spectra in Fig. S2 and 3† exhibit, the elemental proportions of Co, Sn and Fe are extremely similar to the results of ICP-OES.

The detailed structural information was further elucidated by transmission electron microscopy (TEM). The TEM image shows that the produced $CoSn(OH)_6$ perovskite hydroxide has a cube-like shape with a size of approximately 60 nm (Fig. 1f). The $CoSn(OH)_6$ perovskite hydroxide exhibits a closed perpendicular morphology with a uniform contrast, as seen in the high-resolution TEM (HRTEM) image (Fig. 1g). The corresponding fast Fourier transform (FFT) pattern in the inset of

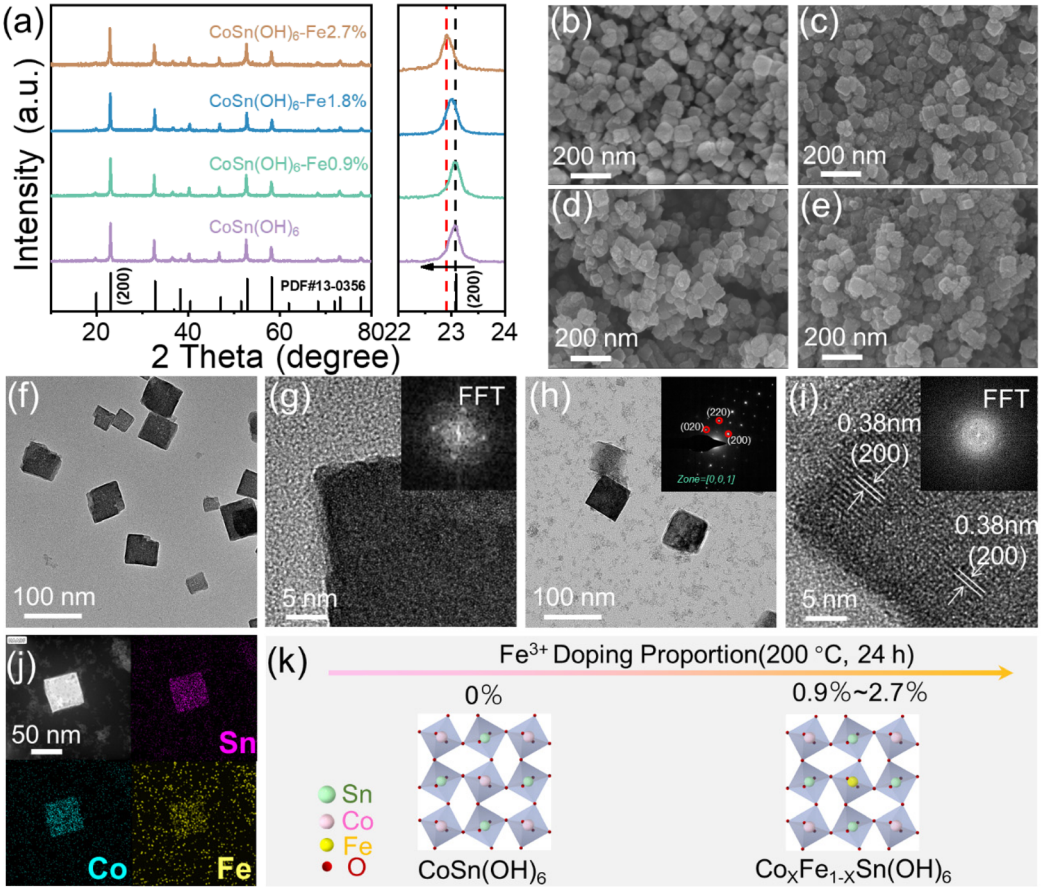

Fig. 1 (a) XRD patterns and SEM (b–e) images of $CoSn(OH)_6$, $CoSn(OH)_6$-Fe0.9%, $CoSn(OH)_6$-Fe1.8%, and $CoSn(OH)_6$-Fe2.7%; (f) TEM image of $CoSn(OH)_6$; (g) HR-TEM image of $CoSn(OH)_6$. The inset is the corresponding FFT diffraction. (h) TEM image and SAED, (i) HR-TEM image (inset is the FFT patterns), and (j) HAADF-STEM images of $CoSn(OH)_6$-Fe1.8% and the EDX elemental maps of Sn, Co, and Fe; (k) the scheme of the structure evolution process of $CoSn(OH)_6$ nanocubes doped with Fe at different proportions.

Fig. 1g reflects that the obtained $CoSn(OH)_6$ exhibits crystallinity.[27] The TEM image of $CoSn(OH)_6$-Fe1.8% shows that the obtained $CoSn(OH)_6$-Fe1.8% perovskite hydroxide has the same morphology as $CoSn(OH)_6$ (Fig. 1h). The corresponding selected area electron diffraction (SAED) pattern shows a set of clear diffraction spots, which can be indexed to the (020), (220), and (200) crystal facets of the perovskite $CoSn(OH)_6$ (inset of Fig. 1h), suggesting the single crystal property of the as-prepared $CoSn(OH)_6$ materials.[41] Furthermore, the HR-TEM image of $CoSn(OH)_6$-Fe1.8% shows that the lattice spacing value is calculated to be 0.38 nm, matching the (200) lattice plane of $CoSn(OH)_6$ (200) (Fig. 1i).[28] According to the FFT pattern, the resulting $CoSn(OH)_6$-Fe1.8% has an octahedral structure (inset of Fig. 1i).[40] In addition, the elemental mapping image of $CoSn(OH)_6$-Fe1.8% from EDX and the high-angle annular dark-field scanning TEM (HAADF-STEM) image in Fig. 1j show that the Co, Sn and Fe elements are homogeneously distributed in $CoSn(OH)_6$-Fe1.8% nanocubes, suggesting that the $CoSn(OH)_6$ nanocubes are evenly doped with Fe^{3+}. The above investigations confirm that we have successfully synthesized the Fe^{3+} doped $CoSn(OH)_6$ nanocubes. The proposed crystal scheme is shown in Fig. 1k, and the Sn, Co, Fe, and O atoms were arranged in the form of a cubic like perovskite structure. The doping of Fe replaces a slight amount of Co.[27]

3.2 Elemental states

The elemental states of the as-prepared $CoSn(OH)_6$ materials were further investigated by X-ray photoelectron spectroscopy (XPS). The C 1s from adventitious carbon (284.8 eV) was used to calibrate the XPS spectra. Fig. 2a displays the Co 2p spectra of $CoSn(OH)_6$ and $CoSn(OH)_6$-Fe1.8%. The centers of Co^{2+} and Co^{3+} states' signal peaks of Co 2p in $CoSn(OH)_6$ are 783.1 and 781 eV, respectively.[42] The centers of Co^{2+} and Co^{3+} states' signal peaks of Co 2p in $CoSn(OH)_6$-Fe1.8% are 782.8 and 780.8 eV, respectively.[43] It demonstrates that $CoSn(OH)_6$-Fe1.8%'s Co 2p binding energy peaks move to a lower energy than that of $CoSn(OH)_6$, which indicates that the electron cloud around the Co atom becomes more concentrated after the incorporation of Fe.[44] Fig. 2b shows the Sn 3d XPS spectra of $CoSn(OH)_6$ and $CoSn(OH)_6$-Fe1.8%. The signal peaks of Sn $3d_{5/2}$ and Sn $3d_{3/2}$ of $CoSn(OH)_6$ are mainly concentrated at 486.6 and 495 eV. In addition, the Sn $3d_{5/2}$ and Sn $3d_{3/2}$ signal peaks of $CoSn(OH)_6$-Fe1.8% are mainly concentrated at 486.5

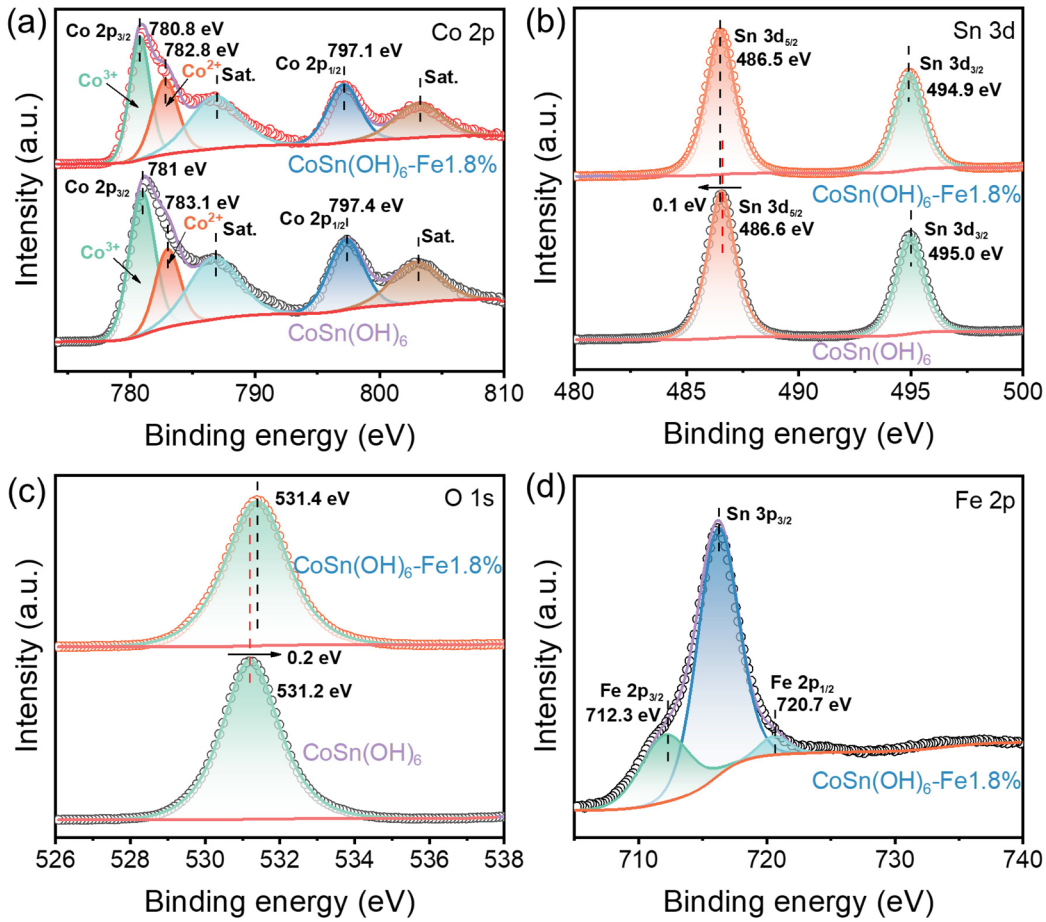

Fig. 2 XPS spectra of (a) Co 2p, (b) Sn 3d, (c) O 1s, and (d) Fe 2p.

and 494.9 eV. Such a result indicates that the main characteristics of Sn^{4+} states exist in $CoSn(OH)_6$ and $CoSn(OH)_6$-Fe1.8% samples.[45] Meanwhile, in comparison with pristine $CoSn(OH)_6$, the 3d orbital energy of Sn^{4+} in the $CoSn(OH)_6$-Fe1.8% sample was negatively shifted, indicating that the electron cloud around the Sn atom becomes thicker after the incorporation of Fe. As shown in Fig. 2c, the peak of fitted curves of $CoSn(OH)_6$-Fe1.8% in the O 1s XPS spectrum is positively shifted in comparison with those of $CoSn(OH)_6$, indicating that the electron cloud around O atom becomes thinner after the incorporation of Fe^{3+}.[46] The existence of the element Fe is thus confirmed by the high-resolution Fe 2p XPS spectrum of the $CoSn(OH)_6$-Fe1.8% sample (Fig. 2d). Th Fe $2p_{3/2}$ and Fe $2p_{1/2}$ of Fe^{3+} are represented by the peaks at 712.3 and 720.7 eV, suggesting the existence of the Fe3+ state.[47] Based on the above analysis, it could be deduced that the Fe^{3+} doping efficiently modulated the electronic structure of $CoSn(OH)_6$.[48]

3.3 Electrocatalytic OER performance

At a scan rate of 10 mV s^{-1}, the catalysts' OER activity was assessed in O_2-saturated 1.0 M KOH (see details in the ESI†). The linear sweep voltammetry (LSV) curves scanned at 10 mV s^{-1} are displayed in Fig. 3a. It can be seen that the Fe^{3+} doped $CoSn(OH)_6$ shows reduced OER overpotentials compared to pristine $CoSn(OH)_6$. The OER activity of Fe^{3+} doped $CoSn(OH)_6$ thus improved gradually along with the Fe^{3+} doping ratio and $CoSn(OH)_6$-Fe1.8% achieved the relatively optimized activity. At a current density of 10 mA cm^{-2}, the overpotential of $CoSn(OH)_6$-Fe1.8% for the OER was determined to be 289 mV. The results show that the electrochemical OER performance of $CoSn(OH)_6$ is significantly influenced by the doping amount of Fe^{3+}. For comparison purpose, the CoFe-LDH ($Co_{0.982}Fe_{0.018}(OH)_x$) was also investigated (Fig. S4†), and $CoSn(OH)_6$-Fe1.8% also shows relatively reduced overpotentials at 10 and 50 mA cm^{-2}, indicating that the perovskite exhibits superior OER activity compared to the corresponding layered hydroxides. The overpotentials at 10 and 50 mA cm^{-2} were compared (Fig. 3b). The highest overpotential of 383 mV was observed in pristine $CoSn(OH)_6$ at a current density of 10 mA cm^{-2}. Otherwise, the OER overpotentials of 325, 289, and 293 mV at 10 mA cm^{-2} were much lower for $CoSn(OH)_6$-Fe0.9%, $CoSn(OH)_6$-Fe1.8%, and $CoSn(OH)_6$-Fe2.7%, respectively. At a current density of 50 mA cm^{-2}, the trend remains the same, where $CoSn(OH)_6$, $CoSn(OH)_6$-Fe0.9%, $CoSn(OH)_6$-Fe1.8%, and $CoSn(OH)_6$-Fe2.7% showed overpotentials of 479, 415, 366, and 436 mV, respectively. According to this analysis, $CoSn(OH)_6$-Fe1.8% possesses optimized electrochemical activity when compared to pristine $CoSn(OH)_6$.[24]

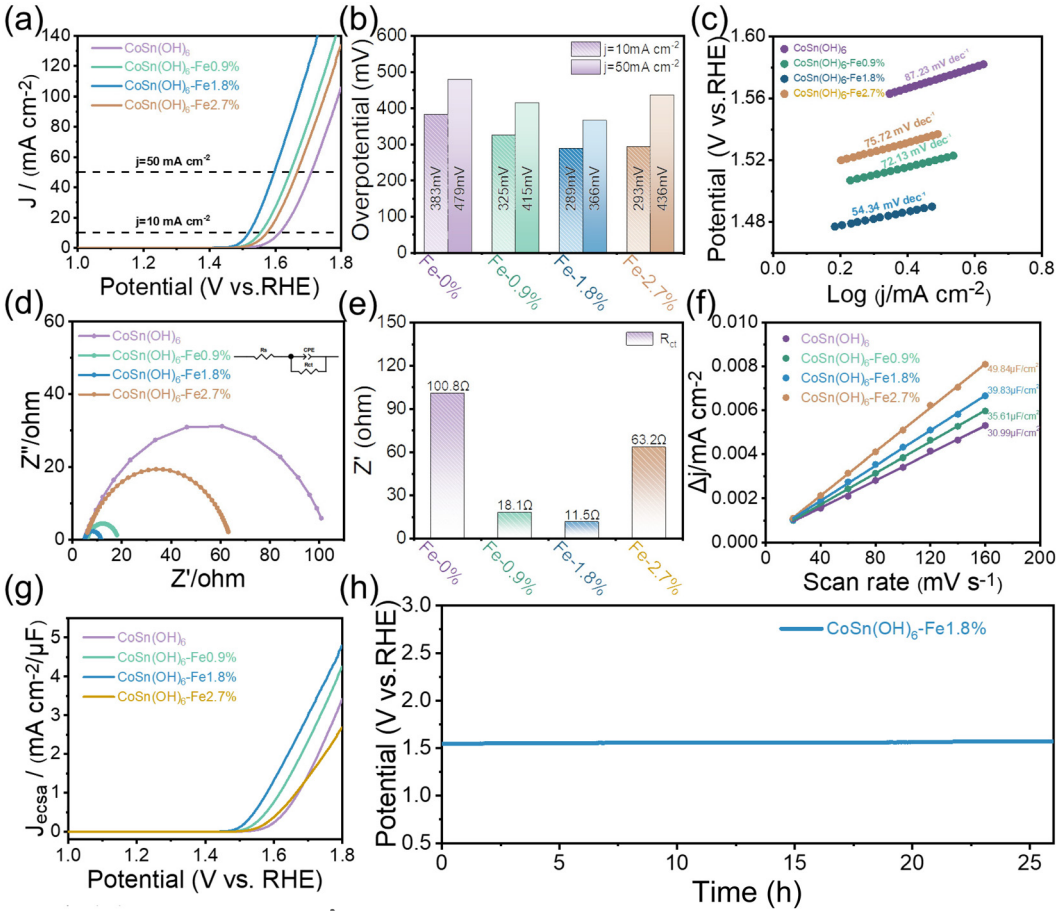

Fig. 3 (a) LSV curves; (b) calculated overpotentials at 10 mA cm^{-2} and 50 mA cm^{-2}; (c) the LSV-derived Tafel slopes; (d) EIS analysis at 1.6 V *vs.* RHE (the inset is the model of the equivalent circuit); (e) impedance values of different samples; (f) current density difference plotted against scan rates; (g) LSV curves normalized with ESCA. (h) Chronopotentiometry curves of $CoSn(OH)_6$-Fe1.8% at 10 mA cm^{-2}.

The Tafel slope (Fig. 3c) was used to determine the OER kinetics of these samples. $CoSn(OH)_6$-Fe1.8% showed the lowest Tafel slope (54.34 mV dec^{-1}) in comparison with $CoSn(OH)_6$-Fe0.9% (72.13 mV dec^{-1}), $CoSn(OH)_6$-Fe2.7% (75.72 mV dec^{-1}), and pristine $CoSn(OH)_6$ (87.23 mV dec^{-1}), confirming that the optimal synthesis conditions are those of the $CoSn(OH)_6$-Fe1.8% product. The electrochemical impedance spectroscopy (EIS) results were obtained at 1.60 V *vs.* RHE (Fig. 3d). Fitting the EIS spectra with an equivalent circuit yields the solution resistance (R_s) and charge transfer resistance (R_{ct}) (inset of Fig. 3d).[27] Every sample has an R_s value of around 6.2 Ω (Table S2†), indicating comparable electrochemical test conditions.[38] The R_{ct} value was obtained by fitting the semicircle at low frequency.[39] As shown in Fig. 3e, the R_{ct} value which represents the charge transfer surface intermediate resistance is ranked in the following order in alkaline electrolyte: $CoSn(OH)_6$-Fe1.8% (11.5 Ω) < $CoSn(OH)_6$-Fe0.9% (18.1 Ω) < $CoSn(OH)_6$-Fe2.7% (63.2 Ω) < $CoSn(OH)_6$ (100.8 Ω). The $CoSn(OH)_6$-Fe1.8% anode thus shows the smallest bulk charge transport resistance. The optimal R_{ct} of $CoSn(OH)_6$-Fe1.8% is beneficial for the charge and mass transfer and during the OER process. In addition, the OER performance of $CoSn(OH)_6$-Fe1.8% and that of already reported Fe, Co, and Sn based materials are compared. The OER activity of the as-prepared $CoSn(OH)_6$-Fe1.8% is comparatively favorable (Table S3†).

The electrochemically active surface area (ECSA) calculated using double-layer capacitance (C_{dl}) is studied to reveal the intrinsic electrocatalytic activity of the Fe^{3+} doped $CoSn(OH)_6$. The CV test conducted between 1.35 and 1.45 V (*vs.* RHE) was used to determine the C_{dl} value (Fig. S5†). As shown in Fig. 3f, the capacitance of $CoSn(OH)_6$, $CoSn(OH)_6$-Fe0.9%, $CoSn(OH)_6$-Fe1.8%, and $CoSn(OH)_6$-Fe2.7% was determined to be 30.99, 35.61, 39.83, and 49.84 μF cm^{-2}, respectively. Then we normalized the LSV curves of Fe^{3+} doped $CoSn(OH)_6$ samples using ECSA, and the Fe^{3+} doped sample still has higher intrinsic activity with the lowest overpotential observed for $CoSn(OH)_6$-Fe1.8% as shown in Fig. 3g. Therefore, Fe^{3+} doping significantly increases the intrinsic activity of $CoSn(OH)_6$ rather than only enhancing the ECSA. Further evaluation of the $CoSn(OH)_6$-Fe1.8% catalyst's durability was conducted using chronopotentiometric (CP) measurement at room temperature and a fixed current density of 10 mA cm^{-2} (Fig. 3h). The potential of $CoSn(OH)_6$-Fe1.8% increases by just 20 mV over 26 hours to maintain a current density of 10 mA cm^{-2}. Meanwhile, the

durability of the $CoSn(OH)_6$-Fe1.8% catalyst was further tested by a chronopotentiometric test at a fixed current density of 100 mA cm^{-2} at room temperature (Fig. S6†), which also shows favorable stability. A comparison of the morphology before and after the electrochemical reactions is shown in Fig. S7.† After the long-term electrochemical measurement, the morphology is almost maintained.

3.4 *In situ* electrochemical characterization

$CoSn(OH)_6$-Fe1.8% and pristine $CoSn(OH)_6$ were characterized by *in situ* Raman spectroscopy in order to gain insights into the structural changes in the electrochemical OER test (Fig. 4a). The carbon fiber paper substrate shows three identical Raman bands at 416, 575, and 749 cm^{-1} (Fig. 4b–c and Fig. S8†). The Co–O vibration in $CoSn(OH)_6$ could be assigned to the other Raman band at 479 cm^{-1}, as demonstrated by the *in situ* Raman spectra of pristine $CoSn(OH)_6$.[49,50] Furthermore, there was no obvious shift in the peak's position nor the appearance of new bands as exhibited in the whole applied potential range. The structure of the $CoSn(OH)_6$ material is stable under the OER process. The $CoSn(OH)_6$-Fe1.8% sample shows the same result, suggesting that the structure is stable during the OER test. There is an extra Raman band (601 cm^{-1}) for the $CoSn(OH)_6$-Fe1.8% sample (Fig. 4c), which is attributed to the Raman band corresponding to the Fe–O vibration from the produced Fe–O (OH).[50,51] The XRD spectra before and after the OER were also examined, which are also consistent with the *in situ* Raman results (Fig. S9†). It is reported that most layered hydroxides materials such as $Ni(OH)_2$ and $Co(OH)_2$ converted into oxyhydroxides (*e.g.* NiOOH and CoOOH) during the OER process.[19,52] For the $CoSn(OH)_6$ material, such a re-construction is not obviously observed, suggesting the superior stability of the perovskite structure during the electrochemical OER process.

3.5 DFT calculations

To further gain deep insight into the influence of Fe^{3+} on the OER performance of $CoSn(OH)_6$, the d-band states were studied using density functional theory calculations (DFT). The corresponding atomic models of $CoSn(OH)_6$ and $Co_{0.83}Fe_{0.17}Sn(OH)_6$ are displayed in Fig. 5a and b. The (001) surfaces of $CoSn(OH)_6$ and $Co_{0.83}Fe_{0.17}Sn(OH)_6$ were constructed to simulate the surface of catalysts, which contained two octahedral layers (Fig. S10†). Fig. 5c and d show the partial density of states (PDOS) of 3d orbitals calculated on the corresponding atomic model.[24,53] The d-band states of these catalysts are near the Fermi level.[30] The electronic structure of the $CoSn(OH)_6$ perovskite hydroxide was changed after Fe^{3+} doping. The calculated d-band centers of $CoSn(OH)_6$, and $Co_{0.83}Fe_{0.17}Sn(OH)_6$ are approximately −2.21 and −1.95 eV, respectively. The value of the d-band center increases after the

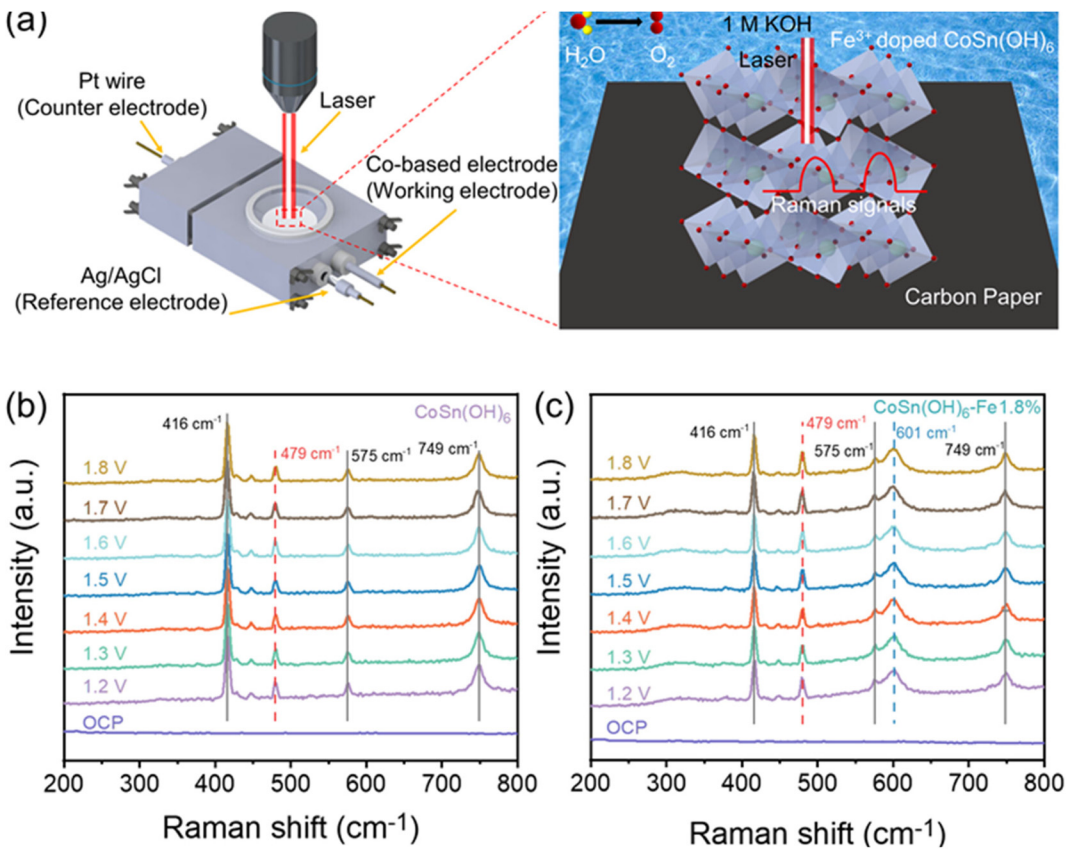

Fig. 4 (a) Schematic illustration of the *in situ* Raman spectroscopy setting; *in situ* Raman spectra of (b) $CoSn(OH)_6$ and (c) $CoSn(OH)_6$-Fe1.8% at different potentials.

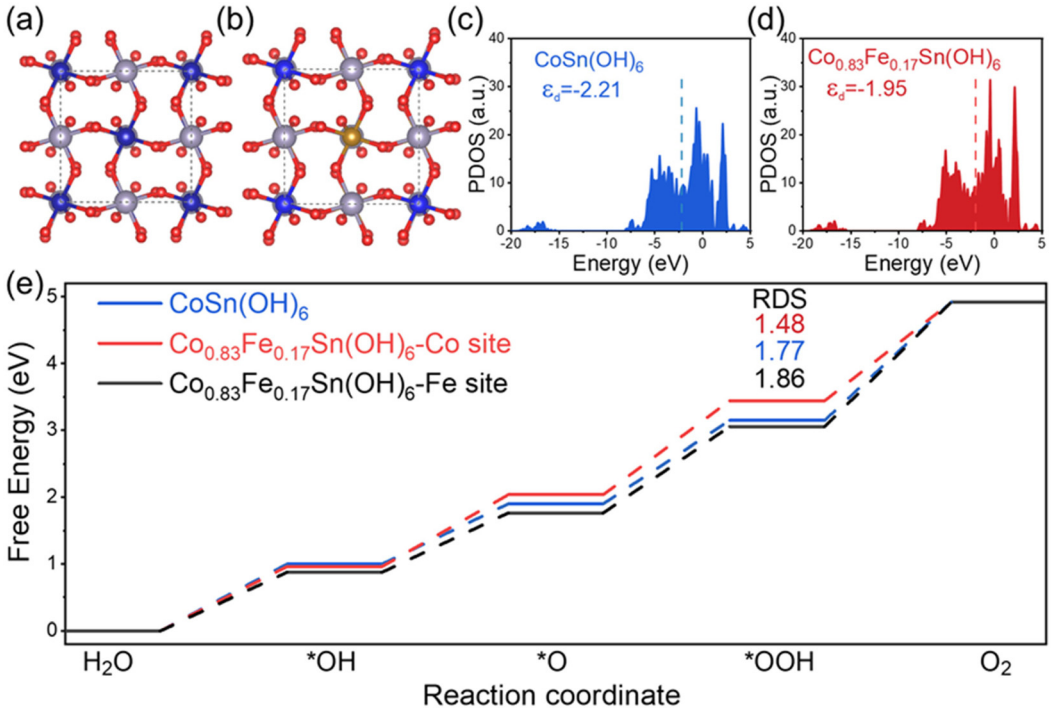

Fig. 5 Schematic changes of the bond structure for (a) $CoSn(OH)_6$ and (b) $Co_{0.83}Fe_{0.17}Sn(OH)_6$; the PDOS of 3d orbitals for (c) $CoSn(OH)_6$, and (d) $Co_{0.83}Fe_{0.17}Sn(OH)_6$; (e) the reaction Gibbs free energy changes during the OER process.

increase of Fe^{3+} content. It is known that the filling degree of the antibonding state can be reflected from the location of the d-band center with respect to the Fermi level.[31] With a higher center of the d band, the antibonding state is filled with fewer electrons, which will result in a stronger bond between the adsorbent and the catalyst.[54] Compared to $CoSn(OH)_6$, the d-band center of the $Co_{0.83}Fe_{0.17}Sn(OH)_6$ perovskite hydroxide is higher, indicating a relatively strong adsorption ability between active sites and intermediates.

In addition, to study the influences of the d-band states on the intermediates' adsorption on these materials, the reaction Gibbs free energies of *OH, *O, and *OOH intermediates

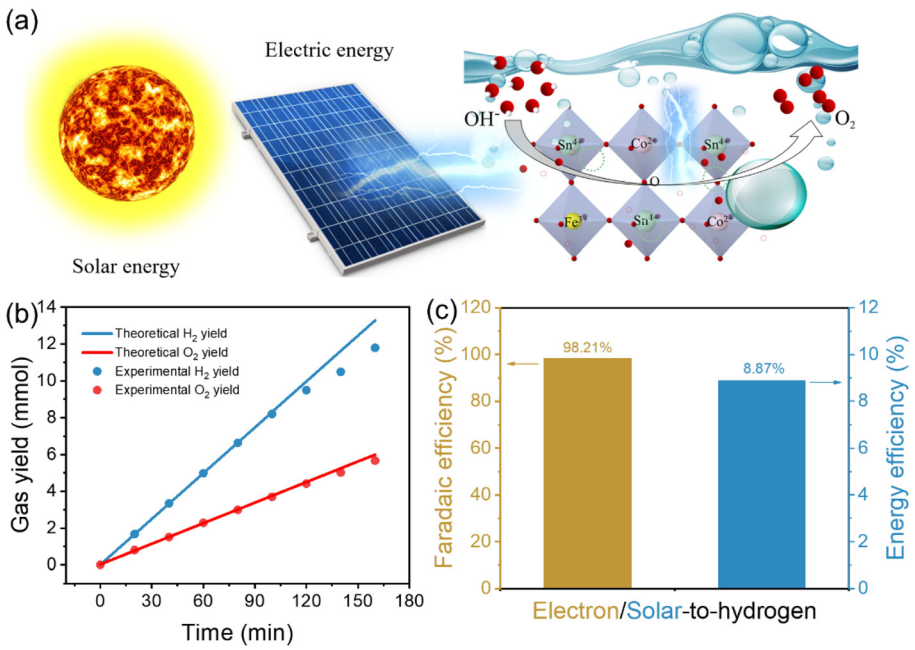

Fig. 6 (a) Schematic of a solar-driven water splitting system; (b) H_2 and O_2 yields for the cathode and anode in 1 M KOH solution; (c) faradaic efficiency and the solar-to-hydrogen energy conversion efficiency at 80 min.

adsorbed on the $Co_{0.83}Fe_{0.17}Sn(OH)_6$ surface were calculated (Fig. S11 and 12†).[55] The Gibbs free energies of *OH, *O, and *OOH at different active sites are displayed in Fig. 5e. The *O to *OOH is the rate-determining step for the various active sites. The Co and Fe sites in the $Co_{0.83}Fe_{0.17}Sn(OH)_6$ perovskite hydroxide require an overpotential of 1.48 eV to adsorb OOH* intermediates following Fe^{3+} substitution, which is lower than that of the Co site in $CoSn(OH)_6$ (1.77 eV). The Fe^{3+} dopants thus can reduce the rate-limiting step's reaction energy barrier and provide a comparatively simple reaction path for the OER.[24,38] Therefore, DFT theoretical calculations show that appropriate Fe^{3+} doping amount can slightly improve the d-band center of the $CoSn(OH)_6$ perovskite hydroxide, which will promote the adsorption ability and reduce the OER reaction energy barrier.

3.6 Solar-driven water splitting

Direct electrolysis of water into hydrogen through the injection of renewable solar energy is the ideal method for producing sustainable energy.[56] In the following study, we built a solar-driven water splitting reaction system by utilizing $CoSn(OH)_6$-Fe1.8% nanocubes as the electrocatalyst for the OER (Fig. 6a). A commercial solar cell was coupled to a two-electrode system and the gas yield during the photovoltaic-electrocatalytic water splitting process was recorded using an online gas chromatograph (Fig. S13† displays the energy conversion system photograph). The light from a Xe lamp was used to simulate sunlight. Fig. S14† displays the Xe lamp's irradiative spectrum. The input solar energy was calculated from the value of light intensity measured using a spectroradiometer (0.309 W cm^{-2}). The actual gas yield is comparable with the theoretical gas yield (Fig. S15†). As Fig. 6b illustrates, the real gas yields of O_2 are approximately half of that of H_2. Furthermore, the faradaic efficiency of evolved H_2 can reach 98.21% (Fig. 6c), and it is still maintained at 87.17% after 160 min (Fig. S16†). Furthermore, about 8.87% was the calculated solar-to-hydrogen energy conversion efficiency (Fig. 6c). The above results show that $CoSn(OH)_6$-Fe1.8% nanocubes are promising for photovoltaic-electrocatalytic water decomposition.

4. Conclusions

In summary, $CoSn(OH)_6$ perovskite hydroxides with tuned d band states by doping varying atomic ratios of Fe^{3+} were achieved. XRD, EDX, and XPS confirmed the successful doping of Fe^{3+} into the $CoSn(OH)_6$ perovskite hydroxide. The optimal Fe^{3+} content was found to be 1.8 mol% ($CoSn(OH)_6$-Fe1.8%), which led to the highest OER activity with an overpotential of 289 mV at 10 mA cm^{-2} in alkaline electrolyte. *In situ* Raman spectroscopy showed that no obvious re-construction occurred during the OER for both $CoSn(OH)_6$ and $CoSn(OH)_6$-Fe1.8%. The DFT-based density of states (DOS) analysis indicated an increase in the d-band center after Fe^{3+} doping. The DFT calculations suggested that incorporation of an appropriate amount of Fe^{3+} into $CoSn(OH)_6$ significantly lowers the Gibbs free energy in the rate-determining step compared to that in pure-phase $CoSn(OH)_6$. In order to evaluate the potential practical application of the as-prepared $CoSn(OH)_6$-Fe1.8%, a photovoltaic-electrolysis water splitting system was established and a solar–hydrogen energy conversion efficiency of 8.87% can be achieved. This study provides an effective strategy to modulate the d-band center of Co-based perovskite hydroxides for a promoted electrocatalytic OER.

Author contributions

Mingwei Sun: conceptualization, data curation, formal analysis, investigation, methodology, writing – original draft, writing – review and editing. Baopeng Yang: formal analysis. Jiaxing Yan: data curation – support, formal analysis – support. Yulong Zhou: validation – support. Zhencong Huang: validation – support. Ning Zhang: funding acquisition, project administration, resources, supervision, validation, writing – review and editing. Rong Mo: review and editing. Renzhi Ma: review and editing.

Conflicts of interest

There are no conflicts to declare.

Acknowledgements

This work received financial support from the National Natural Science Foundation of China (22072183) and the Natural Science Foundation of Hunan Province, China (2022JJ30690 and 2024JJ5378). This work was supported in part by the High Performance Computing Center of Central South University.

References

1 S. Chu and A. Majumdar, *Nature*, 2012, **488**, 294–303.
2 S. Wang, G. Liu and L. Wang, *Chem. Rev.*, 2019, **119**, 5192–5247.
3 Z. W. Seh, J. Kibsgaard, C. F. Dickens, I. Chorkendorff, J. K. Nørskov and T. F. Jaramillo, *Science*, 2017, **355**, eaad4998.
4 K. Jiao, J. Xuan, Q. Du, Z. Bao, B. Xie, B. Wang, Y. Zhao, L. Fan, H. Wang, Z. Hou, S. Huo, N. P. Brandon, Y. Yin and M. D. Guiver, *Nature*, 2021, **595**, 361–369.
5 J. Greeley, T. F. Jaramillo, J. Bonde, I. Chorkendorff and J. K. Nørskov, *Nat. Mater.*, 2006, **5**, 909–913.
6 S. Chu, Y. Cui and N. Liu, *Nat. Mater.*, 2017, **16**, 16–22.
7 N.-T. Suen, S.-F. Hung, Q. Quan, N. Zhang, Y.-J. Xu and H. M. Chen, *Chem. Soc. Rev.*, 2017, **46**, 337–365.
8 Y. He, L. Jia, X. Lu, C. Wang, X. Liu, G. Chen, D. Wu, Z. Wen, N. Zhang, Y. Yamauchi, T. Sasaki and R. Ma, *ACS Nano*, 2022, **16**, 4028–4040.

9 C. C. L. McCrory, S. Jung, I. M. Ferrer, S. M. Chatman, J. C. Peters and T. F. Jaramillo, *J. Am. Chem. Soc.*, 2015, **137**, 4347–4357.
10 L. C. Seitz, C. F. Dickens, K. Nishio, Y. Hikita, J. Montoya, A. Doyle, C. Kirk, A. Vojvodic, H. Y. Hwang, J. K. Norskov and T. F. Jaramillo, *Science*, 2016, **353**, 1011–1014.
11 Y. Chen, H. Li, J. Wang, Y. Du, S. Xi, Y. Sun, M. Sherburne, J. W. Ager, A. C. Fisher and Z. J. Xu, *Nat. Commun.*, 2019, **10**, 572.
12 D. Wang and D. Astruc, *Chem. Soc. Rev.*, 2017, **46**, 816–854.
13 L. Wu, L. Yu, X. Xiao, F. Zhang, S. Song, S. Chen and Z. Ren, *Research*, 2020, **2020**, DOI: 10.34133/2020/3976278.
14 N. Sakai, K. Fukuda, R. Ma and T. Sasaki, *Chem. Mater.*, 2018, **30**, 1517–1523.
15 Y. Hu, F. Li, Y. Long, H. Yang, L. Gao, X. Long, H. Hu, N. Xu, J. Jin and J. Ma, *J. Mater. Chem. A*, 2018, **6**, 10433–10440.
16 X. Xu, F. Song and X. Hu, *Nat. Commun.*, 2016, **7**, 12324.
17 W. Xin, B. Liu, Y. Zhao, G. Chen, P. Chen, Y. Zhou, W. Li, Y. Xu, Y. Zhong and Y. A. Nikolaevich, *Electrochim. Acta*, 2022, **404**, 139748.
18 H. Wan, R. Ma, X. Liu, J. Pan, H. Wang, S. Liang, G. Qiu and T. Sasaki, *ACS Energy Lett.*, 2018, **3**, 1254–1260.
19 S. Liu, R.-T. Gao, M. Sun, Y. Wang, T. Nakajima, X. Liu, W. Zhang and L. Wang, *Appl. Catal., B*, 2021, **292**, 120063.
20 S.-Y. Lee, I.-S. Kim, H.-S. Cho, C.-H. Kim and Y.-K. Lee, *Appl. Catal., B*, 2021, **284**, 119729.
21 D. Zhong, T. Li, D. Wang, L. Li, J. Wang, G. Hao, G. Liu, Q. Zhao and J. Li, *Nano Res.*, 2022, **15**, 162–169.
22 S. Anantharaj, K. Karthick and S. Kundu, *Mater. Today Energy*, 2017, **6**, 1–26.
23 Z. He, J. Zhang, Z. Gong, H. Lei, D. Zhou, N. Zhang, W. Mai, S. Zhao and Y. Chen, *Nat. Commun.*, 2022, **13**, 2191.
24 S. Liu, S. Geng, L. Li, Y. Zhang, G. Ren, B. Huang, Z. Hu, J.-F. Lee, Y.-H. Lai, Y.-H. Chu, Y. Xu, Q. Shao and X. Huang, *Nat. Commun.*, 2022, **13**, 1187.
25 H. Ding, H. Liu, W. Chu, C. Wu and Y. Xie, *Chem. Rev.*, 2021, **121**, 13174–13212.
26 M. A. Peña and J. L. G. Fierro, *Chem. Rev.*, 2001, **101**, 1981–2018.
27 D. Chen, M. Qiao, Y.-R. Lu, L. Hao, D. Liu, C.-L. Dong, Y. Li and S. Wang, *Angew. Chem., Int. Ed.*, 2018, **57**, 8691–8696.
28 Z. Wang, Z. Wang, H. Wu and X. W. Lou, *Sci. Rep.*, 2013, **3**, 1391.
29 J. Suntivich, H. A. Gasteiger, N. Yabuuchi, H. Nakanishi, J. B. Goodenough and Y. Shao-Horn, *Nat. Chem.*, 2011, **3**, 546–550.
30 Z. Chen, Y. Song, J. Cai, X. Zheng, D. Han, Y. Wu, Y. Zang, S. Niu, Y. Liu, J. Zhu, X. Liu and G. Wang, *Angew. Chem., Int. Ed.*, 2018, **57**, 5076–5080.
31 S. Bhattacharjee, U. V. Waghmare and S.-C. Lee, *Sci. Rep.*, 2016, **6**, 35916.
32 H. Zhang, F. Wan, X. Li, X. Chen, S. Xiong and B. Xi, *Adv. Funct. Mater.*, 2023, **33**, 2306340.
33 X. Guo, J. Shi, M. Li, J. Zhang, X. Zheng, Y. Liu, B. Xi, X. An, Z. Duan, Q. Fan, F. Gao and S. Xiong, *Angew. Chem., Int. Ed.*, 2023, **62**, e202314124.
34 X. Guo, J. Zhang, L. Yuan, B. Xi, F. Gao, X. Zheng, R. Pan, L. Guo, X. An, T. Fan and S. Xiong, *Adv. Energy Mater.*, 2023, **13**, 2204376.
35 P. Li, S. Zhao, Y. Huang, Q. Huang, B. Xi, X. An and S. Xiong, *Adv. Energy Mater.*, 2024, **14**, 2303360.
36 X. Guo, M. Duan, J. Zhang, B. Xi, M. Li, R. Yin, X. Zheng, Y. Liu, F. Cao, X. An and S. Xiong, *Adv. Funct. Mater.*, 2022, **32**, 2209397.
37 Z. Xiao, W. Zhou, N. Zhang, C. Liao, S. Huang, G. Chen, G. Chen, M. Liu, X. Liu and R. Ma, *Chem. Commun.*, 2021, **57**, 6070–6073.
38 D. Luo, B. Yang, Z. Mei, Q. Kang, G. Chen, X. Liu and N. Zhang, *ACS Appl. Mater. Interfaces*, 2022, **14**, 52857–52867.
39 S. Chen, Z. Zheng, Q. Li, H. Wan, G. Chen, N. Zhang, X. Liu and R. Ma, *J. Mater. Chem. A*, 2023, **11**, 1944–1953.
40 L. Kang, C. Ye, X. Zhao, X. Zhou, J. Hu, Q. Li, D. Liu, C. M. Das, J. Yang, D. Hu, J. Chen, X. Cao, Y. Zhang, M. Xu, J. Di, D. Tian, P. Song, G. Kutty, Q. Zeng, Q. Fu, Y. Deng, J. Zhou, A. Ariando, F. Miao, G. Hong, Y. Huang, S. J. Pennycook, K.-T. Yong, W. Ji, X. Renshaw Wang and Z. Liu, *Nat. Commun.*, 2020, **11**, 3729.
41 F. Song, K. Schenk and X. Hu, *Energy Environ. Sci.*, 2016, **9**, 473–477.
42 N. S. McIntyre and M. G. Cook, *Anal. Chem.*, 1975, **47**, 2208–2213.
43 H. Lyu, D. Yin, B. Zhu, G. Lu, Q.-Y. Liu, X. Zhang and X. Zhang, *ACS Sustainable Chem. Eng.*, 2020, **8**, 9404–9414.
44 S. Riyajuddin, K. Azmi, M. Pahuja, S. Kumar, T. Maruyama, C. Bera and K. Ghosh, *ACS Nano*, 2021, **15**, 5586–5599.
45 R. Sahoo, A. K. Sasmal, C. Ray, S. Dutta, A. Pal and T. Pal, *ACS Appl. Mater. Interfaces*, 2016, **8**, 17987–17998.
46 L. Zhuang, L. Ge, Y. Yang, M. Li, Y. Jia, X. Yao and Z. Zhu, *Adv. Mater.*, 2017, **29**, 1606793.
47 X. Jiang, W. Xu, R. Tan, W. Song and J. Chen, *Mater. Lett.*, 2013, **102–103**, 39–42.
48 M. Liu, K.-A. Min, B. Han and L. Y. S. Lee, *Adv. Energy Mater.*, 2021, **11**, 2101281.
49 J.-Z. Zhang, Z. Zhang, H.-B. Zhang, Y. Mei, F. Zhang, P.-X. Hou, C. Liu, H.-M. Cheng and J.-C. Li, *Nano Lett.*, 2023, **23**, 8331–8338.
50 W. H. Lee, M. H. Han, Y.-J. Ko, B. K. Min, K. H. Chae and H.-S. Oh, *Nat. Commun.*, 2022, **13**, 605.
51 X. Xing, C. Wu, G. Yang, T. Tong, Y. Wang, D. Wang, F. C. Robles Hernandez, Z. Ren, Z. Wang and J. Bao, *Mater. Today Chem.*, 2022, **26**, 101110.
52 S. She, Y. Zhu, H. A. Tahini, X. Wu, D. Guan, Y. Chen, J. Dai, Y. Chen, W. Tang, S. C. Smith, H. Wang, W. Zhou and Z. Shao, *Small*, 2020, **16**, 2006800.
53 W. Wu, S. Shi, Z. Zhang, X. Guo, L. Sun, R. Wei, J. Zhang, L. Gao, X. Pan and G. Xiao, *J. Colloid Interface Sci.*, 2022, **619**, 407–418.

54 J. Liu, H. Liu, H. Chen, X. Du, B. Zhang, Z. Hong, S. Sun and W. Wang, *Adv. Sci.*, 2020, **7**, 1901614.
55 N. Zhang, B. Yang, Y. He, Y. He, X. Liu, M. Liu, G. Song, G. Chen, A. Pan, S. Liang, R. Ma, S. Venkatesh and V. A. L. Roy, *Small*, 2018, **14**, 1803015.
56 T. Faunce, S. Styring, M. R. Wasielewski, G. W. Brudvig, A. W. Rutherford, J. Messinger, A. F. Lee, C. L. Hill, H. deGroot, M. Fontecave, D. R. MacFarlane, B. Hankamer, D. G. Nocera, D. M. Tiede, H. Dau, W. Hillier, L. Wang and R. Amal, *Energy Environ. Sci.*, 2013, **6**, 1074–1076.